(Received 10 February 2026, Accepted 9 March 2026, Scheduled 14 May 2026)

Hybrid Genetic Optimization of Metasurfaces for Scattering Control: X-Band Design and Experimental Validation

Sandro Marzullo, Ilaria Marasco*, Antonella D'Orazio, and Giovanni Magno

Department of Electrical and Information Engineering, Politecnico di Bari, Italy

ABSTRACT: The design of large-scale coding metasurfaces poses significant computational challenges, often limited by the prohibitive time required for full-wave simulations necessary for optimization. This paper proposes an efficient design strategy based on a Hybrid Genetic Algorithm, validated through the design, fabrication, and characterization of an X-band metasurface for Radar Cross Section reduction. The proposed design strategy relies on a two-stage optimization process: a fast pre-optimization phase, based on the analytical Huygens-Fresnel principle, generates a preliminary solution which is subsequently refined by a second optimization stage utilizing full-wave simulations. Specifically, the optimization targets a 1-bit coding scheme, where meta-atoms switch between two distinct states with a phase difference of $180 \pm 37^{\circ}$. This hybrid approach demonstrates optimal convergence, reducing computational time by 25% compared to traditional full-wave-only techniques. Furthermore, a novel "spiralling cross" unit cell topology is introduced. Owing to its delay-line geometry, this structure provides additional degrees of freedom for spectral tuning and supports intermediate phase shifts, thus enabling encoding schemes beyond traditional 1-bit configurations. Experimental results confirm the validity of the proposed approach, demonstrating how the combination of versatile geometry and hybrid optimization effectively overcomes the trade-offs between numerical accuracy and computational efficiency.

1. INTRODUCTION

Metasurfaces have revolutionized electromagnetic engineering by offering unprecedented control over the wavefront through 2D arrays of sub-wavelength scatterers. In particular, coding metasurfaces have gained attention for their ability to bridge wave physics and digital information theory, enabling scattering manipulation by tailoring the spatial distribution of logical 'bits'. However, the synthesis of such structures poses a significant computational challenge because determining the optimal distribution of meta-atoms requires exploring vast and discrete search spaces.

Within this context, one of the most compelling applications of coding metasurfaces is radar cross-section (RCS) reduction. In modern electromagnetic surveillance systems, the ability to control and reduce the RCS of a target has become a fundamental requirement for the development of advanced stealth platforms for military and civilian applications [1]. RCS is a key parameter for quantifying the detectability of an object [2], and it is formally defined as the effective area that intercepts incident power density and produces the same scattered power observed at the radar receiver, when isotropically reradiated. The RCS is not solely determined by the physical size of the target but is also strongly influenced by factors such as the geometry of the structure, the electromagnetic properties of the constituent materials, and surface features including edges, joints, and protrusions, which act as scattering centers [3]. Reducing the RCS directly translates into lower radar visibility, making it a fundamental parameter of stealth technology. Accordingly, RCS reduction has become a critical requirement for design objectives for low-observable platforms across multiple domains, ranging from tactical aircraft and naval vessels to space systems and Unmanned Aerial Vehicles (UAVs) [4, 5]. The growing dependence on autonomous platforms and satellite assets for reconnaissance, navigation, and communication has further underscored the importance of electromagnetic signature control, highlighting its relevance not only for survivability in contested environments but also for resilience in civilian and dual-use applications [6]. Early RCS reduction strategies primarily relied on geometric shaping, where platform contours were engineered to deflect incoming radar waves away from the source, thereby minimizing backscatter. These methods were frequently combined with radar-absorbing materials, which dissipate incident electromagnetic energy as heat, as well as with structural features designed to diffuse or redirect scattering [3]. While effective, these techniques suffer from significant drawbacks: they tend to increase structural weight, exhibit limited bandwidth, and impose strict mechanical constraints. Such limitations make them less suitable for the broadband, lightweight, and multifunctional platforms required in modern operational scenarios [7, 8]. Over the last decade, metasurfaces have emerged as one of the most promising solutions for RCS reduction, also within the X-band [9–11]. These structures consist of two-dimensional arrays of subwavelength scatterers that provide control over electromagnetic wave manipulation [12, 13]. Metasurfaces can be designed to precisely control reflection, absorption, and scattering, by tailoring the geometry, arrangement, and electromagnetic response of the unit cells [14]. Several mechanisms can be exploited to achieve RCS reduction.

* Corresponding author: Ilaria Marasco (ilaria.marasco@poliba.it).

One approach relies on the destructive interference of reflected waves, where unit cells are engineered to impose specific phase shifts that cancel backscattered signals in the monostatic direction [15, 16]. Another strategy involves polarization conversion, which transforms incident wave into its orthogonal polarization. Since radar receivers are typically optimized for co-polarized returns, this conversion leads to an apparent reduction in detectability [17]. Another method is diffuse scattering, which is achieved by introducing spatial randomness or pseudo-random coding into the metasurface arrangement, redistributing the backscattered energy over multiple directions and thereby reducing the intensity in the radar's line of sight [18]. Finally, broadband absorption can be achieved by integrating resistive films, lumped elements, or multilayer lossy substrates, enabling the effective dissipation of electromagnetic energy across a wide frequency range [19, 20]. Among these, the most impactful solution is the coding metasurface, which redefines the design process within a digital framework: each unit cell is modeled as a digital "bit", with discrete states corresponding to specific reflection phase levels. A 1-bit coding metasurface employs two states (typically 0° and 180°), while multi-bit designs incorporate more states to achieve finer phase resolution [21]. By arranging these coded elements into optimized patterns, metasurfaces can suppress direct backscatter and generate customized scattering distributions [22, 23]. This approach not only simplifies the design process but also facilitates integration with digital optimization techniques, where coding sequences can be directly represented as chromosomes in evolutionary algorithms [24]. Recent works have proposed tailored meta-atom geometries that provide phase differences close to 180° across broad frequency ranges, enhancing bandwidth while maintaining compact designs. For example, Ameri et al. [25] introduced dual artificial magnetic conductor unit cells exhibiting phase shifts of $180° \pm 37°$, achieving RCS reductions greater than 10 dB over an approximately 85% fractional bandwidth. Similarly, Haji-Ahmadi et al. [7] developed pixelated checkerboard metasurfaces optimized via topology-based methods, experimentally demonstrating more than 10 dB of RCS reduction from 3.8 to 10.7 GHz with angular stability up to 40°. However, such pixel-based optimizations often lead to highly irregular meta-atom shapes, complicating fabrication. Designing coding metasurfaces remains a challenging task, especially in large arrays containing hundreds or thousands of elements with multiple discrete states. Brute-force search is computationally prohibitive, and conventional gradient-based optimization methods are ineffective due to the discrete and multimodal nature of the problem [26]. To overcome these issues, Genetic Algorithms (GAs) and other evolutionary approaches have been widely adopted [27]. GAs mimic natural selection through operations, such as mutation, crossover, and selection, allowing them to efficiently explore large, complex design spaces and avoid the presence of local minima. Furthermore, GAs are inherently suited for multi-objective optimization, enabling simultaneous improvements in broadband performance, polarization independence, angular stability, and robustness to fabrication tolerances [28, 29]. Their integration with surrogate modelling and parallel computation has further expanded their applicability, making them practical tools for addressing the high computational demands of metasurface optimization [24]. Surrogate-assisted strategies reduce the computational burden of full-wave simulations by employing simplified models or data-driven approximations during optimization. While machine learning approaches provide predictive capabilities, they require large training datasets and preprocessing [30, 31], which can limit their application in custom design scenarios. Similarly, adjoint methods offer gradient-based optimization for continuous parameters but face challenges when applied to discrete or binary-coded metasurfaces, where the lack of gradient information for discrete states necessitates binarization or spatial filtering techniques [32]. The hybrid optimization strategy proposed in this work employs a physics-based analytical approximation derived from the Huygens-Fresnel principle as a low-fidelity model for solution-space exploration. This is followed by a high-fidelity full-wave refinement stage, providing a framework that balances computational efficiency with the accuracy required to capture electromagnetic interactions. While GAs effectively explore complex design spaces, their efficiency is strictly linked to the cost of the fitness function evaluation. Relying on rigorous full-wave solvers ensures accuracy but incurs prohibitive time costs. Conversely, approximate analytical models accelerate calculation but tend to fail at high frequencies where mutual coupling is non-negligible.

To bridge this gap, this paper introduces a design strategy based on a Hybrid Genetic Algorithm (HGA). The approach relies on a two-stage optimization process: a rapid pre-optimization phase, based on the analytical Huygens-Fresnel Principle (HFP), generates a preliminary solution which is subsequently refined by a second optimization stage utilizing full-wave simulations (using a finite-element solver). This hybrid strategy reduces the computational time by 25% compared to traditional full-wave-only techniques, effectively balancing numerical accuracy and efficiency.

Parallel to this, the present paper introduces a novel meta-atom geometry, referred to as the "spiraling-cross". Owing to its C4-symmetric geometry incorporating meandered delay lines, this structure provides enhanced degrees of freedom for spectral tuning, enhanced phase tunability and inherent polarization insensitivity with a compact, single-layer design compatible with standard printed circuit board (PCB) fabrication processes. Specifically, we identify two distinct highly reflective configurations of the spiraling-cross unit cell that exhibit a phase difference close to 180°, serving as the '0' and '1' bits. Using these states, the HGA determines the optimal spatial coding matrix to minimize the RCS across the X-band (8–12 GHz). Notably, the performance of the proposed hybrid strategy was benchmarked against two reference approaches: a GA relying solely on the analytical Huygens-Fresnel Principle (HFP), and a GA driven exclusively by full-wave simulations. We show that the HFP-only GA converges to a trivial chessboard pattern, whereas the hybrid full-wave refinement captures mutual coupling effects,leading to a non-trivial coding distribution comparable to the full-wave-only solution but obtained in significantly less time. The resulting metasurface exhibits substantial RCS reduction throughout the X-band while preserving polarization independence and fabrication simplicity, offering a favorable

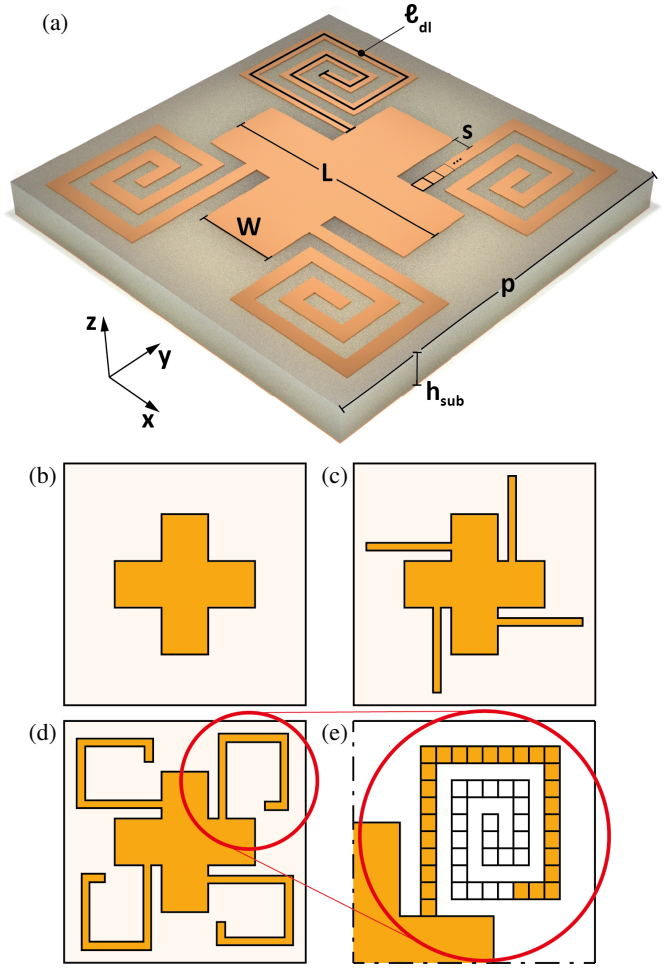

FIGURE 1. (a) Three-dimensional view of the unit cell with the spiralling cross pattern. (b) Central cross resonator. (c) Cross resonator with four initial delay-line stubs. (d) Intermediate stage of the spiral delay-line construction. (e) Polyomino-based implementation of the delay line, obtained by sequentially joining square elements into a total length of ℓ_{dl}.

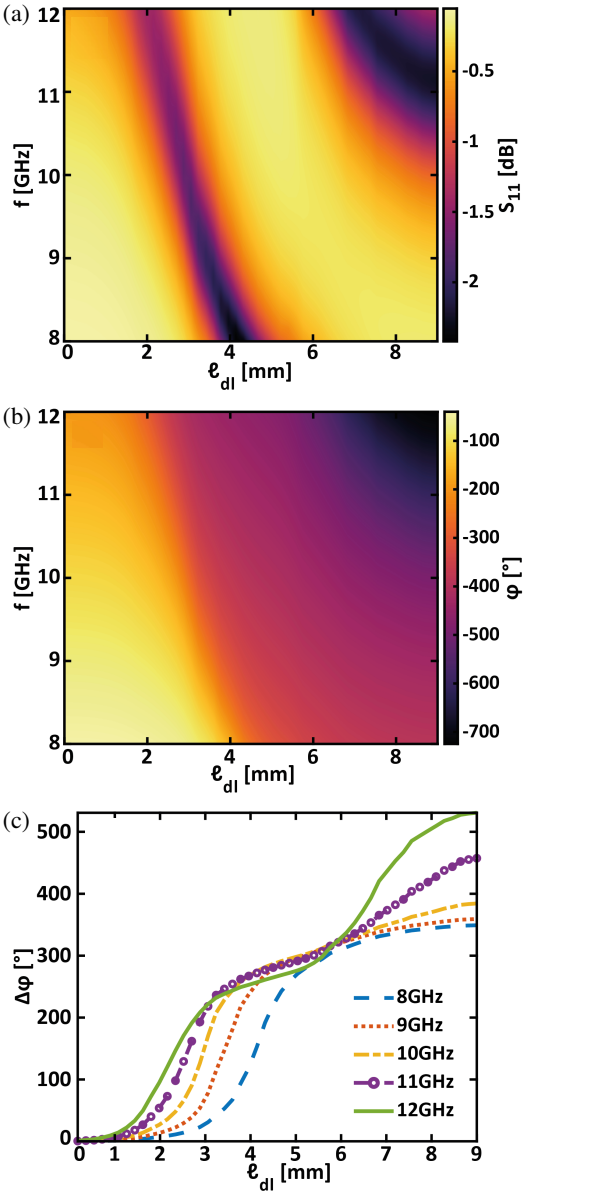

FIGURE 2. (a) Magnitude and (b) phase ϕ of S_{11} for the unit cell under normal incidence and TE polarization, as a function of the frequency and delay-line length ℓ_{dl}. (c) Phase ϕ at selected frequencies.

trade-off among performance, computational cost, and structural robustness in the design of RCS-reduction metasurfaces. In addition, to validate the numerical results and evaluate the experimental feasibility of the proposed structure, a prototype of the optimized metasurface was fabricated on an FR-4 substrate using an LPKF ProtoMat S104 milling system. The fabricated sample was characterized through two-port scattering-parameter measurements in a controlled setup, enabling the experimental assessment of its angular and spectral behavior.

2. STRUCTURES AND METHODS

The unit cell is designed on an FR-4 substrate of thickness h_{sub}, while copper layers of thickness h_{Cu} form both the ground plane and the patterned top surface, as shown in Fig. 1(a). The square unit cell, of period p, features two resonant elements on its top layer: (i) a central cross-shaped resonator with arm widths W and arm lengths L, (ii) four C4-symmetric spiral delay lines emanating from the cross arms. Each delay-line, of length ℓ_{dl}, is constructed by sequentially joining 0.18×0.18 mm squares to form a polyomino that extends 9 mm, forming a spiral-like pattern as shown in Figs. 1(b)–(e). All dimensions are reported in Table 1. The central cross dimensions and the period determine the overall spectral position of the structure's resonances within the target frequency band. The delay-line length ℓ_{dl} progressively shifts the resonance towards lower frequencies as ℓ_{dl} increases, spanning the 8–12 GHz range. The unit-cell period was set to $p = 6$ mm, corresponding to approximately $\lambda/4$ at 12 GHz, in order to guarantee sub-wavelength operation across the entire X-band (8–12 GHz). This choice prevents the excitation of higher-order diffraction modes in free space, ensures proper spatial sampling of the phase distribution (Nyquist criterion), and represents a practical compromise between fabrication feasibility and electromagnetic performance. After fixing the period, the cross dimensions are fixed so that, with

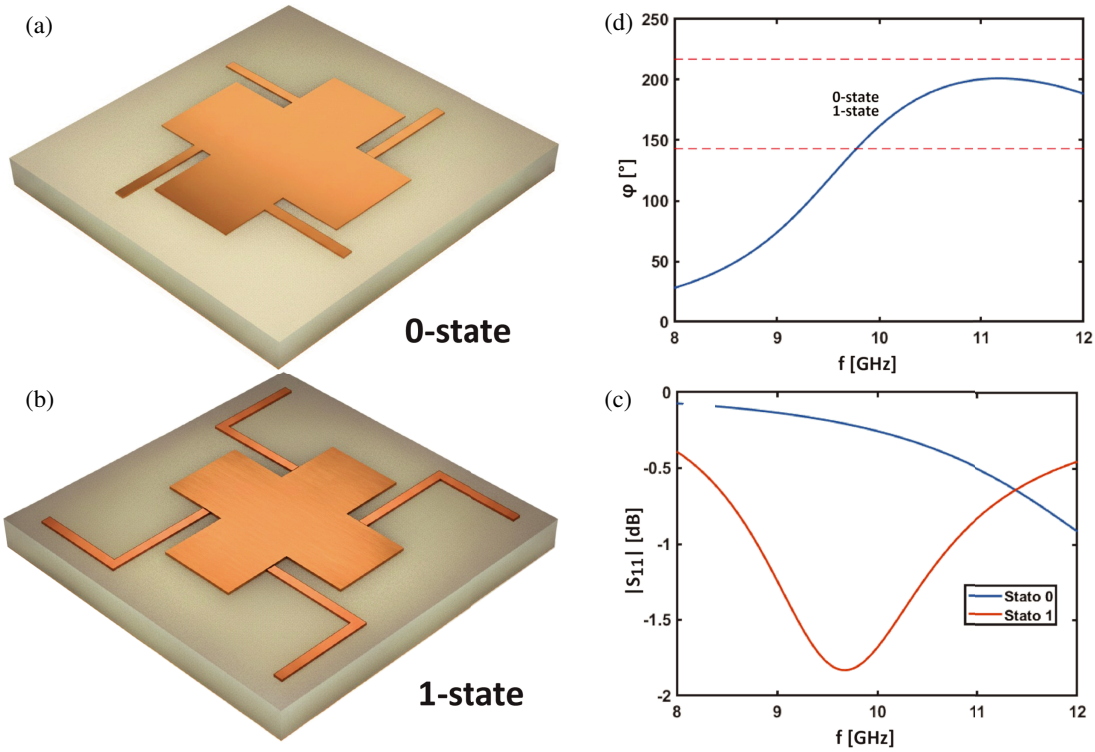

FIGURE 3. (a) (b) Geometry of states 0 and 1 of the unit cell. (c) Comparison of S_{11} for states 0 and 1 (TE polarization). (d) Phase difference between states 0 and 1 (TE polarization).

zero-length delay lines, the targeted resonance is positioned just above the upper edge of the observation window. The scattering parameters under normal incidence are then computed via CST simulations as a function of delay-line length, in order to identify the amplitude and phase excursions of the unit cell. Fig. 2(a) shows the magnitude of the scattering parameter $|S_{11}|$ in decibels for TE polarization at normal incidence, as a function of the frequency and the delay-line length ℓ_{dl}. This map highlights a strong reflectance at $\ell_{dl} = 0$. Owing to symmetry, the TM response was identical. Moreover, the resonance frequency is strongly dependent on ℓ_{dl}. For lengths between approximately 2 and 4 mm, the first resonance sweeps across the entire spectral window. For ℓ_{dl} greater than approximately 7 mm, a second resonance emerges and progressively shifts to lower frequencies as ℓ_{dl} increases. This shift was accompanied by a significant phase excursion of S_{11}, as shown in Fig. 2(b). The effect is further illustrated in Fig. 2(c), which reports phase — ℓ_{dl} curves at equally spaced frequencies from 8 to 12 GHz in 1 GHz increments. Consequently, the unit cell provides a phase span of $180 \pm 37°$ and offers intermediate values, thereby enabling multi-bit (beyond 2-bit) coding. This parametric investigation of the unit cell revealed that increasing the spiral length modified the reflection phase response, with the phase shift between consecutive configurations gradually increasing. This characteristic behavior allows the identification of two states whose relative phase difference lies within the prescribed interval $180 \pm 37°$, while preserving sufficiently low reflection coefficients (in dB).

In checkerboard-type metasurfaces and in the absence of mutual coupling between unit cells, effective scattering cancellation is achieved when adjacent elements reflect waves with similar amplitudes and a phase difference close to 180°. By requiring the residual reflected power to be at least 10 dB below the reference level, the corresponding phase-difference interval becomes approximately $180° \pm 37°$ [25, 33]. These two states can then be unequivocally associated with binary coding, being assigned to the '0' and '1' states, respectively. In this way, the design methodology not only satisfies the phase requirement essential for RCS reduction, but also establishes a rigorous framework for encoding metasurfaces into discrete, digitally addressable states. The selected states, 0 and 1 correspond to the geometries shown in Figs. 3(a) and (b), respectively, with ℓ_{dl} of 1.62 mm for the first case and ℓ_{dl} of 3.24 mm for the second. It is worth noting that, because of symmetry, the structure is invariant under TE or TM polarization. The phase difference between states 0 and 1 (see Fig. 3(d)) meets the $180 \pm 37°$ criterion at frequencies above approximately 10 GHz and extends to frequencies beyond 12 GHz.

TABLE 1. Geometric parameters of the unit cell.

Parameter	Value (mm)	Description
W	1.7	Cross width
L	4	Cross length
h_{Cu}	0.035	Copper thickness
h_{sub}	1.55	Substrate thickness
p	6	Unit cell period
ℓ_{dl}	9	Total loop length

3. DESIGN METASURFACE

In the absence of mutual coupling among adjacent unit cells and assuming identical reflection amplitudes for each element, a metasurface composed of binary states ("0" and "1", inducing phase shifts of 0 and π, respectively) yields a radiation pattern that can be expressed by the superposition principle as

$$E(\vartheta,\varphi) = E_{\text{uc}}(\vartheta,\varphi)\sum_{m,n=0}^{N-1}\exp\{j[kp\sin(\vartheta)(m\cos(\varphi) + n\sin(\varphi)) + \Phi(m,n)]\}. \quad (1)$$

In this formulation, $E(\vartheta,\varphi)$ represents the far-field radiated by the entire metasurface, whereas $E_{\text{uc}}(\vartheta,\varphi)$ is the angular response of a single unit cell. Variables ϑ and φ denote the elevation and azimuth angles, respectively. The parameter N indicates the number of unit cells along each direction of the square lattice, and p is the lattice period. The wavenumber is defined as $k = 2\pi/\lambda$, where λ is the operating wavelength. Finally, $\Phi(m,n)$ specifies the phase term (0 or π) assigned to the unit cell located at the indices (m,n). In Eq. (1), which is adopted in the analytical Huygens-Fresnel pre-optimization stage, the scattered field is described as the superposition of local elementary contributions under the assumptions of identical local response and absence of mutual coupling, with the coding acting only through the binary phase term $\Phi(m,n)$. Under these ideal conditions, periodic checkerboard-like configurations naturally satisfy the destructive-interference condition in the specular direction and are therefore favored by the analytical optimization. In the actual finite metasurface, however, mutual coupling and edge effects make the local contribution of each element dependent on its surrounding environment, introducing perturbations in both amplitude and phase with respect to the ideal response assumed in Eq. (1). These effects are inherently taken into account exclusively in the full-wave optimization stage, where the entire metasurface is simulated. As a result, the ideal checkerboard cancellation is no longer strictly preserved, and full-wave optimization is required to refine the preliminary coding sequence, a process that tends to favor more irregular coding distributions to redistribute the scattered energy over multiple directions more effectively and obtain a final configuration with improved physical accuracy. For completeness, a detailed discussion of coupling effects in related metasurface architectures is reported in [22].

The metasurface can be regarded as a spatially programmable array, in which each unit cell is assigned either state "0" or state "1". This binary representation provides the necessary degrees of freedom to control the far-field radiation pattern. The metasurface design involves binary encoding, where state 0 is associated with bit 0, and state 1 is associated with bit 1. In this framework, the entire design process is reduced to defining a binary matrix in which each entry specifies whether a unit cell is in state 0 or state 1. MATLAB is used to script the binary matrices and, through the CST API, automatically build the corresponding geometrical layouts directly within the CST Microwave Studio. This approach streamlines the creation of complex patterns and facilitates FEM-based simulation. The unit cell was simulated in CST

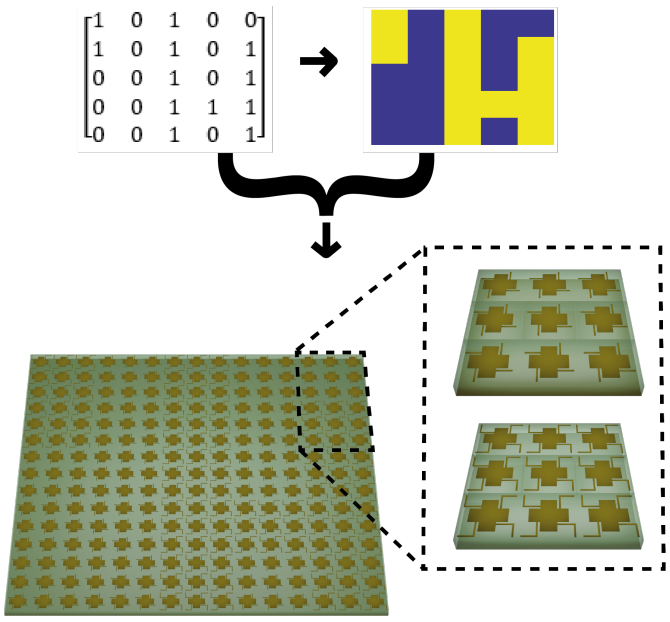

FIGURE 4. Design workflow of the metasurface: a binary matrix defines the spatial distribution of states "0" and "1", each representing a 3×3 block of unit cells. The pattern is scripted in MATLAB and built in CST Microwave Studio. The zoomed views show the two block configurations, corresponding to states "0" and "1".

Microwave Studio under periodic boundary conditions, ensuring that its response correctly represented an infinite periodic array in both frequency- and time-domain analyses. Each entry of the MATLAB binary matrix represents a 3×3 group of unit cells, all programmed in the same state (0 or 1). These groups, each measuring 18×18 mm, were combined to form the overall metasurface as a 5×5 arrangement of such blocks, yielding a total size of 90×90 mm. The overall procedure is illustrated in Fig. 4. This framework is well-suited for RCS minimization using a two-step genetic algorithm [34]. The first step analytically computes the electric field scattered by the metasurface using the HFP to obtain the radiation pattern and the RCS. Each metasurface element is treated as an isotropic radiator, with amplitude and phase characteristics defined by the unit cell state at the desired frequency. We employed the Calc-ScatPat [35] implementation of the HFP in Matlab to compute the scattered field and evaluate the RCS as given in Eq. (2) and reported in [36].

$$\sigma_t = \frac{1}{4\pi}\int_{\phi_s=0}^{2\pi}\int_{\theta_s=0}^{\pi}\sigma(\theta_s,\phi_s)\sin(\theta_s)d\theta d\phi \quad (2)$$

The cost function used in the optimization process is defined as R/R_0, where R is the area subtended by the RCS-versus-frequency curve associated with the considered coding configuration over the frequency range of interest, and R_0 is the corresponding reference area for the worst-case condition, defined by a unitary RCS over the same frequency range. Therefore, the cost function provides a band-integrated measure of the scattering performance: the lower the ratio R/R_0, the lower the overall RCS over the target bandwidth. This formulation enables

the genetic algorithm to identify coding patterns with reduced broadband scattering.

To assess whether the analytical evaluation of the scattered field from the metasurface could provide a reliable first-order estimation, a comparison was conducted between the electric field distribution obtained through the analytical method and that obtained from the full-wave CST simulation. Both cases correspond to the same metasurface configuration derived from an optimization procedure guided solely by analytical data. All of the simulations were executed on a desktop computer equipped with an Intel i9-13900K CPU (3 GHz, 24 cores) and 128 GB of DDR4 RAM.

Figure 5 reports a direct comparison of the far-field patterns at 8, 10, and 12 GHz obtained from the checkerboard configuration (Fig. 5(g)), which will be further discussed later as it represents the solution provided by the genetic algorithm optimization guided solely by the analytical data. At 8 GHz, the analytical pattern (Fig. 5(a)) is very similar to the CST result (Fig. 5(d)). However, as the frequency increases, the agreement deteriorates. At 10 GHz, the two patterns diverge, particularly in amplitude (see Fig. 5(b) vs Fig. 5(e)), and at 12 GHz, the mismatch becomes significant (see Fig. 5(c) vs Fig. 5(f)). This behavior reflects the increased importance of the mutual-coupling effect at higher frequencies, which is neglected in the analytical calculation. Therefore, it provides only a qualitative estimate of the fields.

Three different applications of the genetic algorithm are investigated here for the optimization of the metasurface pattern. In all cases, the algorithm was implemented using the MATLAB Optimization Toolbox. Fig. 6 displays the flowcharts corresponding to the three applications. In the first application, the genetic algorithm was initialized with a population size of 50, using a Gaussian mutation function with a scaling factor of 2 and a shrink factor of 3.5. These settings maximize the diversity of the population, allowing a wider exploration of the solution domain and reducing the risk of local minima occurrence. The RCS was analytically evaluated using the HFP. The corresponding flowchart is reported in Fig. 6(a).

The algorithm stops by stall generation after a computation time of 25 minutes, and the solution found has a cost function value of 11.69, where the cost function is defined as the ratio of the RCS area of the specific pattern R to that of the worst case R_0.

In the second application, the algorithm is executed on the same system, and the genetic algorithm is directly driven by CST simulation of the metasurface patterns, using the same parameters as in the second case (population size 50, Gaussian mutation with scaling actor 1 and shrink 0.5) for consistency. The corresponding flowchart is reported in Fig. 6(b). The genetic algorithm terminates by stall generation after a computation time of 4 days, reaching a cost function value of 5.68.

In the third application, the algorithm is first guided by the analytical evaluation and then refined using full-wave simulations of the metasurface in CST. The corresponding flowchart is reported in Fig. 6(c). In this case, the genetic algorithm starts from the best population obtained in the analytical phase, with a population size of 50 and a Gaussian mutation function (scaling factor 1, shrink factor 0.5) to keep individuals closer to the starting solution. This strategy prevents successive populations from drifting too far, yet avoiding the stagnation that an overly broad search could induce. Consequently, the second phase acts as a refinement stage that polishes the solutions already obtained. The algorithm stops after a computation time of 3 days, as shown in Table 2, achieving a cost function value of 5.66.

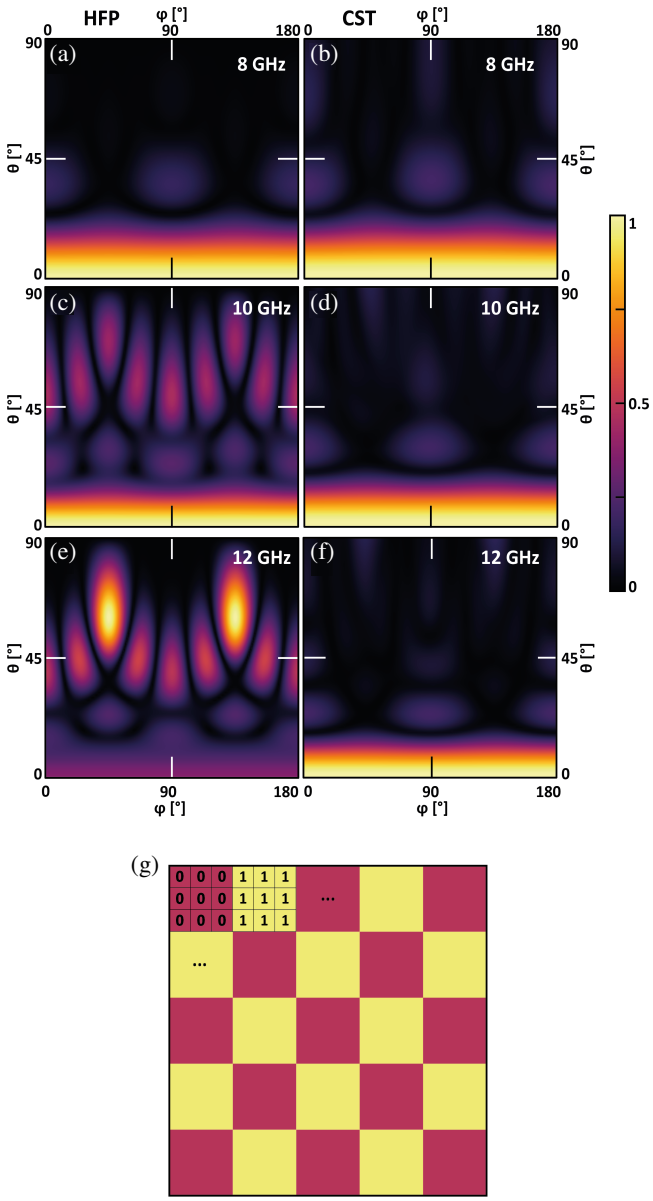

FIGURE 5. Normalized far-field amplitude patterns of the metasurface at (a) (d) 8 GHz, (b) (e) 10 GHz, and (c) (f) 12 GHz. In (a)–(c), the patterns are obtained with the Huygens-Fresnel Principle (HFP) method, while (d)–(f) are full-wave results from CST. (g) Sketch of the checkerboard programming of the metasurface states. All maps report the normalized magnitude of the radiated electric field $|E|$ [V/m] as a function of azimuth ϕ and elevation θ.

A comparison between the second and third applications shows that the CST-HFP scheme (second case) leads to shorter computation time and slightly better solutions in terms of the cost function. Table 2 summarizes the parameters used in the three different optimization schemes, including the population

TABLE 2. Comparison of the genetic algorithm settings, computation times, and final cost-function values for the three optimization schemes.

	HFP	HFP + CST	CST
Population size	50	50	50
Mutation (Scale, Shrink)	(2, 3.5)	(1, 0.5)	(1, 0.5)
Stop Criteria (Stall G)	30	5	5
Computation Time	25 minutes	3 days	4 days
Cost function ($\frac{R}{R_0}$)	11.69	5.66	5.68

size, the mutation parameters, and the stopping criteria, and also reports the computational times required and the final value of the cost function. As reported above and summarized in Table 2, the hybrid HFP + CST optimization requires about 3 days, whereas the CST-only optimization takes about 4 days on the same hardware platform (Intel i9-13900K CPU with 128 GB RAM), corresponding to a computational time reduction of approximately 25%.

4. SIMULATION, RESULTS, AND DISCUSSION

A comparison between the configurations obtained with the GA guided solely by the analytical data and those resulting from the hybrid and full-wave optimizations revealed clear differences. These are illustrated in Fig. 7, which reports the optimized binary encoding of the metasurface and the corresponding far-field electric field patterns at 8, 10, and 12 GHz. In the first case, corresponding to the genetic algorithm guided only by analytical data and shown in Fig. 7(a), the solution systematically converged towards a checkerboard-like arrangement. This behavior can be explained by the fact that the analytical approach neglects the mutual coupling among unit cells, thereby inherently favoring regular and periodic arrangements. In contrast, when the optimization process includes full-wave simulations, either in the hybrid version, as shown in Fig. 7(b), or in the full CST version, as shown in Fig. 7(c), the genetic algorithm converges towards random-like distributions, which prove to be more effective in reducing the RCS. This improvement stems from the ability of random patterns to spread the reflected energy more uniformly and suppress the formation of strong directive lobes.

Another important aspect is the convergence time of the proposed methods. The convergence behavior can be evaluated by tracking the mean penalty and best penalty metrics, as shown in Figs. 8(a) and (b). A key observation lies in the comparison between the hybrid method and the one solely driven by CST data: while the hybrid method starts from a higher initial penalty value, it converges within significantly shorter computation times than the latter. This highlights how analytical analysis can serve as an effective pre-processing stage, guiding the genetic algorithm toward more relevant regions of the solution space, reducing redundant searches, and ultimately improving convergence efficiency.

The RCS performance results for the three cases are reported in Fig. 9, which shows the RCS values as a function of frequency for the three optimization approaches, with reference to the RCS produced by an aluminum surface of the same size as the metasurfaces. It can be observed that the HFP + CST method provides significant improvements over the version based solely on HFP, extending the operational band-

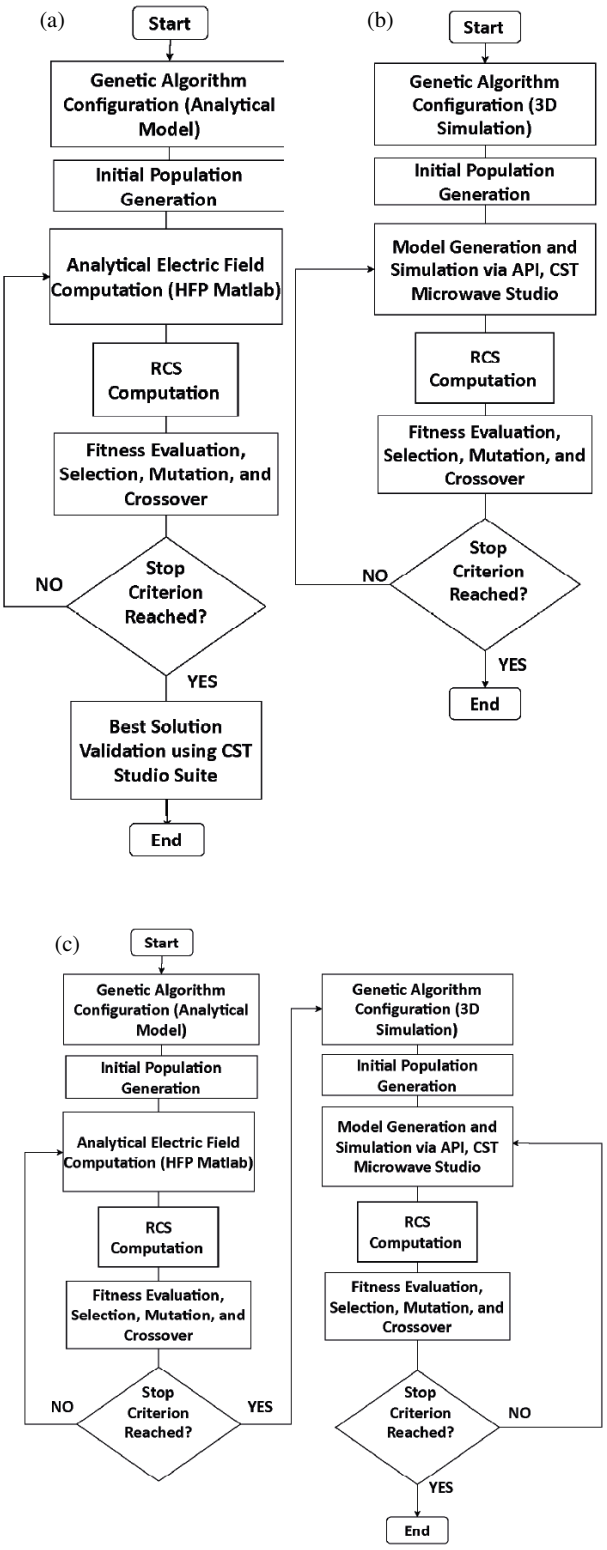

FIGURE 6. Flowcharts of the three optimization approaches based on genetic algorithms: (a) genetic algorithm driven solely by the analytical data; (b) genetic algorithm driven solely by CST simulation data; (c) genetic algorithm with pre-processing on analytical data followed by post-processing on CST simulation data.

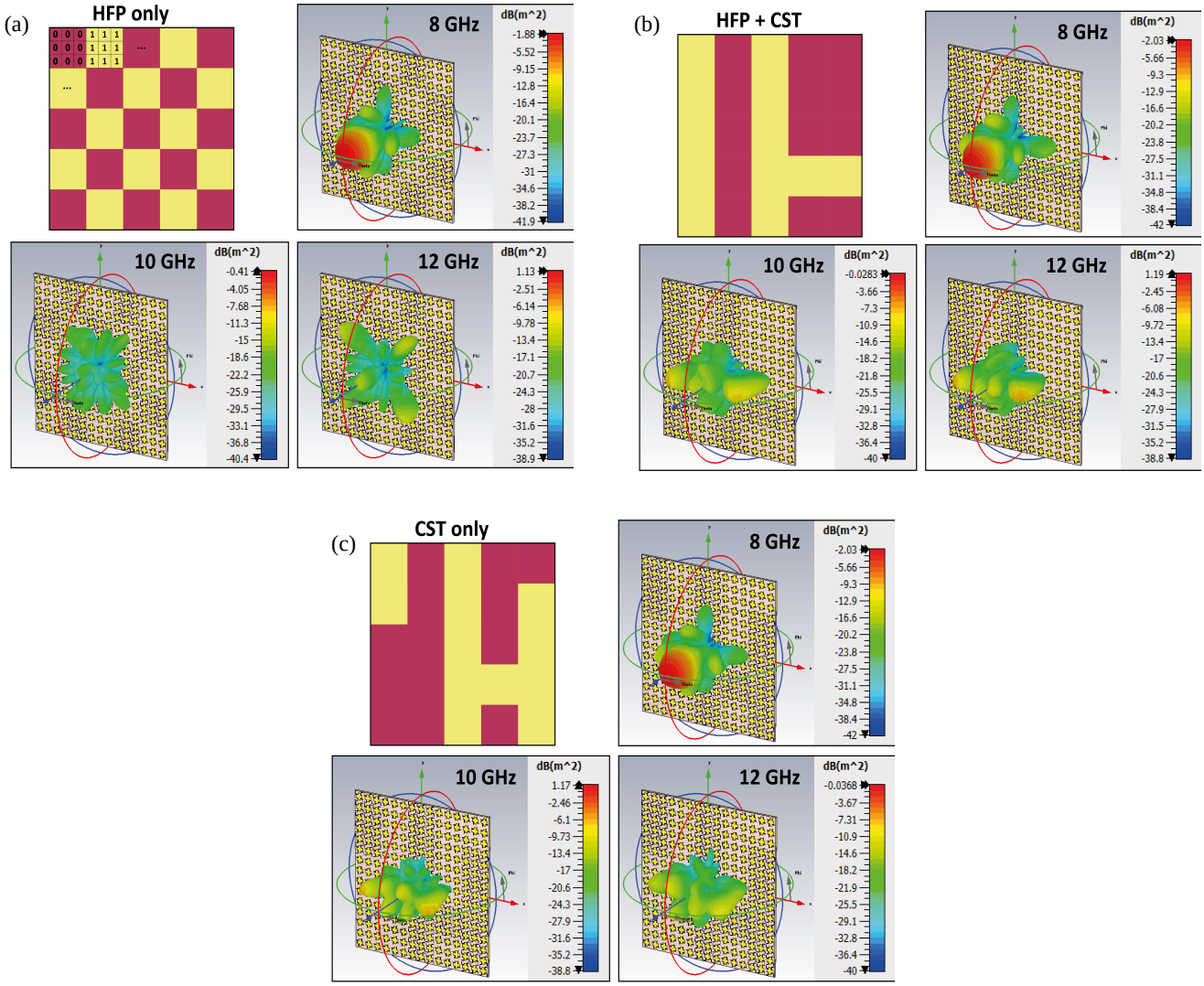

FIGURE 7. Binary maps and 3D electric field distributions at 8, 10, and 12 GHz for the three optimization approaches: (a) GA guided by analytical data only; (b) GA guided by analytical data with CST-based post-processing and (c) GA guided by CST data only.

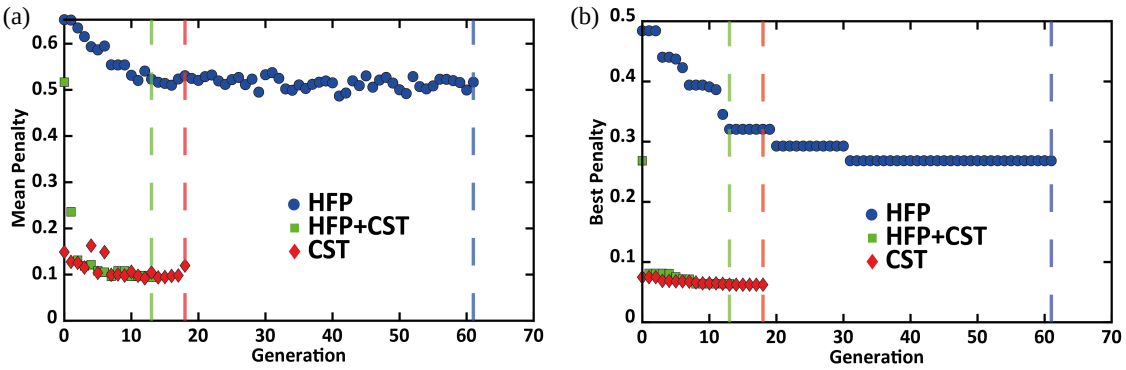

FIGURE 8. Output metrics of the genetic algorithm: (a) mean penalty vs. generations; (b) best penalty vs. generations. Colors indicate different approaches: blue corresponds to GA guided by analytical data only, green to hybrid optimization, and red to GA guided solely by CST simulations.

width across the entire 9–12 GHz range. Moreover, it yields results comparable to the CST-only approach, while requiring significantly shorter computation times. Quantitatively, Fig. 9 shows that, for the HFP + CST method, the optimized metasurface achieves a maximum RCS reduction of about 21.17 dB around 10 GHz, while the average RCS reduction across the 9–12 GHz band is about 11.76 dB with respect to the reference metallic plate. The outcomes of the last two cases are consistent with the phase difference between the two cell states, which meets the requirement of $180° \pm 37°$ within the 9–12 GHz

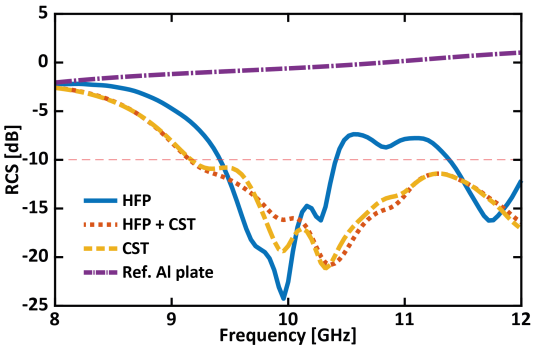

FIGURE 9. RCS as a function of frequency, with reference to an aluminum surface of equal size (shown in purple). Colors indicate different optimization approaches: blue corresponds to analytical data only, orange to analytical data with CST post-processing, and yellow to CST data only.

range, thereby fully exploiting the characteristics of the two cells.

Finally, compared with the existing literature (see Table 3), it can be observed that many works aim at broadband solutions, often relying on complex geometries or large-size arrays. In this context, the approach proposed in this paper is characterized by the simplicity of the unit cell and the compact size of the analyzed array (90×90 mm), while still achieving comparable RCS reduction within the frequency band of interest. The achieved RCS-reduction bandwidth is primarily limited by the dispersive response of the adopted unit cells and by the limited number of phase states available in the binary (1-bit) coding scheme. Furthermore, the compact size of the metasurface, required to satisfy experimental constraints that will be discussed later, could also limit the achievable RCS-reduction performance compared with larger metasurfaces.

TABLE 3. Comparison of the performance of alternative methods for RCS reduction, including the fractional bandwidth (FBW) corresponding to the reported −10 dB bandwidth.

REF	−10 dB BW (GHz)	FBW (%)	Area (mm^2)	RCS method
[18]	8.6–22.5	89.4	264×264	AMC
[37]	8–23.65	98.9	204×204	PCR
[38]	15.5–34.6	76.2	144×144	Geometry
[39]	4–18.25	128.1	200×200	Conductivity
This work	9–12	28.6	90×90	Geometry

From an optimization perspective, extending the proposed framework to multi-bit coding metasurfaces would increase the number of discrete states associated with each unit cell and, consequently, enlarge the search space explored by the genetic algorithm. Although this would likely increase the overall computational cost, the hybrid HFP + CST strategy would remain beneficial in limiting the number of expensive full-wave evaluations.

To experimentally validate the RCS-reduction performance predicted by the hybrid HFP-CST optimization, the metasurface corresponding to the optimal binary pattern was fabricated on FR-4 using an LPKF ProtoMat milling machine. A reference plate sample consisting of an unpatterned FR-4 substrate with identical dimensions was fabricated to provide a baseline for comparison. The resulting samples are shown in Fig. 10. Both samples were characterized in an anechoic chamber using a bistatic goniometric measurement setup. This bistatic configuration was adopted for experimental characterization because the proposed metasurface reduces detectability mainly through angular redistribution of the scattered energy, whereas a monostatic measurement would provide information only in the backscattering direction. The measurement configuration employed two X-band aluminum horn antennas (Arra Inc., 8.2–12.4 GHz) featuring rectangular apertures of 6.68 cm × 8.89 cm and nominal gains between 15 and 18 dBi. The antennas were positioned at a fixed distance of approximately 1 m from the sample under test and connected to the two ports of a Keysight FieldFox N9917A vector network analyzer. The VNA was calibrated using open, short, and load standards prior to the measurements in order to ensure measurement accuracy and repeatability.

Before the angular measurements, the setup was manually aligned using the metallic reference sample placed at the measurement position. In the first step, the reference surface was kept parallel to the transmitting horn aperture, and the horn height and orientation were adjusted to maximize the reflected signal $|S_{11}|$. In the second step, the transmitting and receiving antennas were positioned at 45° with respect to the reference surface, and the receiving antenna was fine-tuned to maximize S_{21}. After completing the alignment, the reference sample was replaced with the fabricated metasurface, and the S_{21} parameter was recorded along the circumference corresponding to $\theta = 0^\circ$. The angular scan was performed by varying ϕ from 5° to 70° in steps of 5°, thus covering the first quarter of the circumference. The scan was limited to 70° because at 90°, the two antennas would be orthogonal, a condition in which the received power becomes negligible. The second quarter of the circumference was obtained by rotating the metasurface by 180° and repeating the same scan in ϕ. This rotation is equivalent to scanning ϕ from -5° to -70°, allowing acquisition of the symmetric angular region without modifying the measurement setup. This procedure enables the reconstruction of the full angular response while keeping the geometry of the setup fixed. The simulated and experimental measurement setup are illustrated in Fig. 11: Fig. 11(a) shows the CST-based simulated setup, while Fig. 11(b) presents the experimental setup implemented in the anechoic chamber. Owing to the limited length of the goniometric arm, which is constrained by the internal dimensions of the anechoic chamber, the measurement was carried out at a distance that was close to, but did not fully satisfy the conventional far-field condition for the X-band horns. To consider the effects of the residual presence of near-field and intermediate-field components, as well as the finite aperture of the antennas, the identical measurement geometry was reproduced in CST. Fig. 12 reports the angular-frequency maps of the transmitted coefficient S_{21} obtained for both the reference FR-4 plate and the optimized metasurface, comparing the CST simulations (left column) with the experimental measurements (right column). Figs. 12(a) and (b) correspond to the

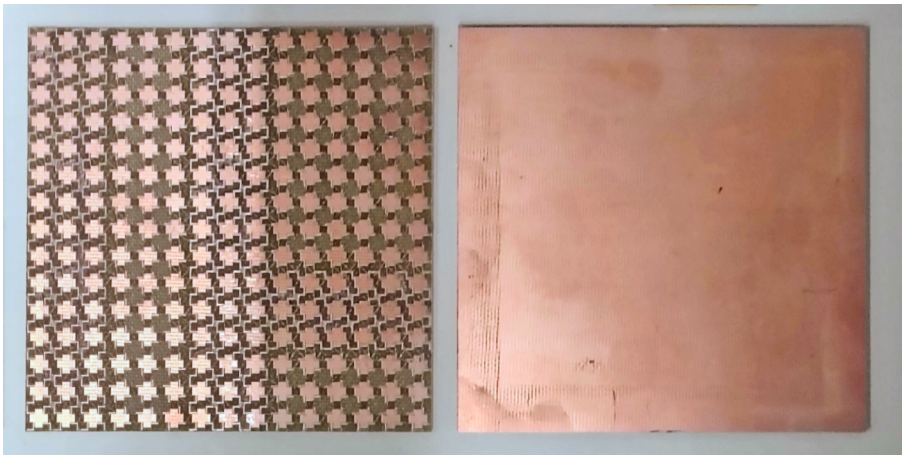

FIGURE 10. Comparison between the metasurface and the reference plane.

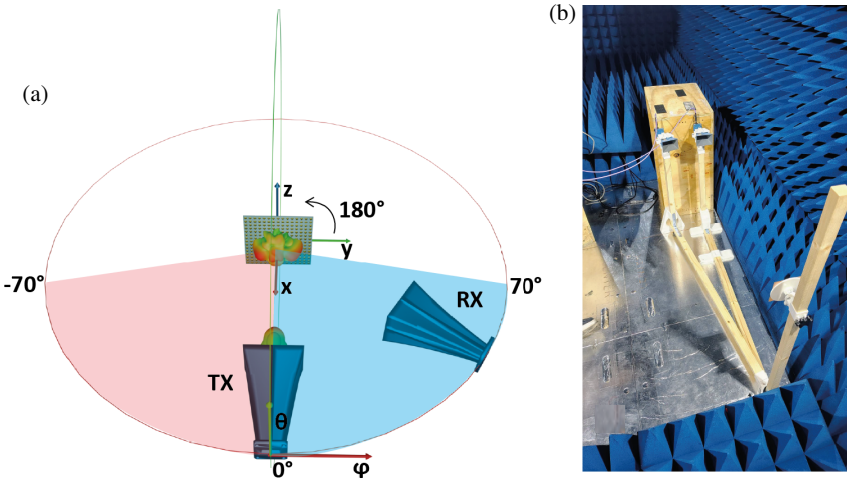

FIGURE 11. (a) CST simulation of the measurement setup used to acquire the S_{21} parameter. The blue arc represents the scan performed with the metasurface in its initial orientation, corresponding to ϕ varying from 5° to 70°. The red arc indicates the scan obtained after a 180° rotation of the metasurface, which is equivalent to acquiring S_{21} for ϕ ranging from $-5°$ to $-70°$; (b) Experimental measurement setup implemented in the anechoic chamber.

unpatterned reference sample, whereas Figs. 12(c) and (d) refer to the fabricated metasurface. In all cases, S_{21} is plotted as a function of the receiving-arm angle θ (from $-70°$ to $+70°$) and frequency in the 8–12 GHz range. In the adopted bistatic configuration, the received power at the second antenna is proportional to the squared magnitude of the scattered electric field generated by the sample. Since the bistatic RCS is defined from the same scattered-field quantity, the measured S_{21} maps provide a qualitative indication of the angular redistribution of the scattered field. Therefore, the measured maps are intended to validate the bistatic scattering pattern produced by the metasurface, rather than to retrieve absolute RCS values. For comparison, a metallic plate with the same lateral dimensions as the fabricated sample was also measured under the same conditions; this metallic plate was used only as a benchmark case and not for normalization.

For the reference FR-4 plate (Figs. 12(a), (b)), the simulated and measured maps exhibit consistent features: a strong, almost frequency-independent (a minor broadening is visible at the lowest frequencies) feature centered at $\theta = 0°$, corresponding to the main lobe of the transmitting horn reflected by the reference plate; in addition, several weaker secondary lobes are visible at larger angles, arising from the actual radiation pattern of the transmitting horn, whose finite aperture and directive nature produce a characteristic radiation pattern. A slight narrowing of the main lobe is observed when measured against the simulated result. This behavior can be attributed to the actual horn antenna, whose effective radiating aperture is slightly smaller than that of the antenna model assumed in the numerical configuration. Aside from the presence of measurement noise at the lower S_{21} levels, the overall angular dependence and frequency response are well reproduced experimentally. The metasurface results (Figs. 12(c)–(d)) show the characteristic redistribution of the transmitted energy over a broader set of angles, as expected from the RCS-reduction design. The measured S_{21} map qualitatively matches the simulated one, displaying compara-

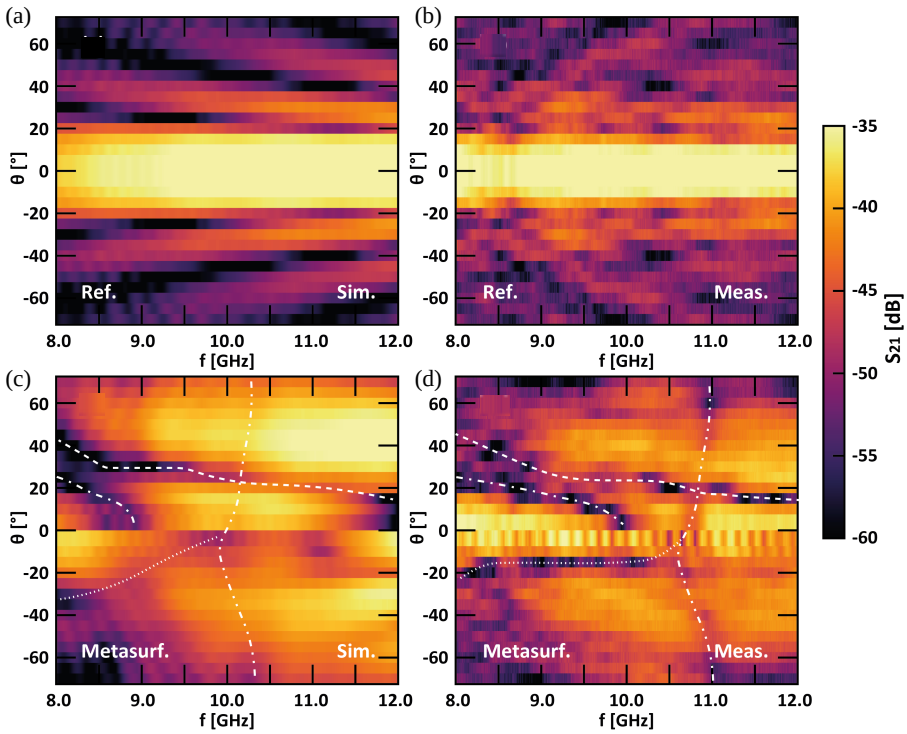

FIGURE 12. Maps of the S_{21} parameter as a function of the receiving-arm angle θ and frequency, for both the reference FR-4 plate and the optimized metasurface. (a) and (c) show the CST simulations for the reference plate and the metasurface, respectively; (b) and (d) report the corresponding measurements. In (c) and (d), purely qualitative hand-traced dashed curves that approximately follow the local S_{21} minima are added solely to aid visual identification of the dominant angle-frequency features and to ease comparison between simulated and measured maps.

ble angular spreading and similar amplitude levels. A noticeable difference, however, appears to be a spectral blueshift of approximately 1 GHz in the measured features relative to the simulated map.

In the CST model, the FR-4 substrate was described by a nominal relative permittivity $\varepsilon_r = 4.3$ and loss tangent $\tan\delta = 0.02$. The discrepancy between the simulated and measured bistatic S_{21} maps in Fig. 12 is not interpreted here as the rigid shift of a single resonance, but rather as a perturbation of the overall angle-frequency scattering response. Additional sensitivity analyses, not presented here for conciseness, showed that varying ε_r mainly redistributes the scattering features over the bistatic map, whereas a reduction in the realized trace width produces a moderate shift of the dominant features toward higher frequencies. A better qualitative agreement with the measured map was obtained only when both effects were considered together. Therefore, the observed mismatch is reasonably attributed to the combined effect of uncertainty in the effective dielectric properties of FR-4 and fabrication tolerances of the realized copper pattern.

Despite this shift, the measured angular distribution remains consistent with the simulation, confirming the metasurface's ability to diffuse the transmitted field over multiple angles and frequencies. The measurement uncertainty is mainly associated with manual alignment and positioning tolerances, which primarily affect the $|S_{21}|$ level rather than the angular trend of the measured scattering maps. The repeatability of the setup was evaluated through 30 repeated measurements, leading to a conservative expanded uncertainty below 2 dB over the investigated frequency band.

For clarity, a set of hand-drawn dashed curves has been superimposed on the maps to guide the visual identification of the most prominent S_{21} features, which approximately follow the local minima. These curves are purely qualitative and were traced by manually following the valleys in the angle-frequency plane, with the sole purpose of highlighting the main scattering features and facilitating the comparison between simulated and measured responses. It is worth noting that neither the simulated nor the measured response at $\theta = 0°$ is shown in the maps. This is due to the geometric constraints of the measurement setup, which prevent the horns from approaching closer than $\pm 5°$ without physical contact. Moreover, measurements taken at small angles exhibit a comb-like sequence of evenly spaced resonances (≈ 0.15 GHz), originating from a 1 m-long Fabry-Pérot cavity formed between the metasurface and the receiving horn aperture. The same phenomenon is also present in the CST simulations, although it appears less pronounced in the numerical results.

5. CONCLUSIONS

This paper presents an efficient design strategy for coding metasurfaces, validated by addressing the specific application of radar cross-section (RCS) reduction in the X-band. Three optimization approaches were compared: (i) an analytical-only approach, (ii) a full-wave-only optimization, and (iii) the proposed Hybrid Genetic Algorithm (HGA). The results highlight

a limitation of relying solely on the analytical Huygens-Fresnel principle: by neglecting mutual coupling, the algorithm tends to converge towards trivial checkerboard patterns. Conversely, the hybrid strategy offers an interesting trade-off: it yields non-trivial coding distributions with scattering diffusion properties comparable to those obtained by full-wave-only optimization, while reducing the total computational time by 25%. The numerical design obtained using the hybrid genetic algorithm was fabricated and characterized. The measurements were compared with the numerical simulation, showing good agreement with a limited frequency shift attributable to manufacturing tolerances. Although the fabricated prototype has limited dimensions due to experimental constraints related to the measurement setup and far-field requirements, the proposed coding framework is inherently scalable and can be extended to significantly larger metasurfaces. For larger arrays, the relative influence of edge effects is expected to become less pronounced, while the statistical properties of the optimized coding distribution increasingly dominate the scattering behavior. Regarding the unit cell, the adopted "spiralling-cross" topology incorporates meandered delay lines that allow continuous phase tuning. Although this work implemented a 1-bit coding scheme ($0°/180°$), the cell response supported intermediate phase shifts. Future developments of the proposed optimization framework may include its extension to multi-bit coding metasurfaces, which could provide additional phase states and potentially improve the achievable bandwidth, making it suitable for applications involving programmable metasurfaces.

ACKNOWLEDGEMENT

This work was supported by the European Union under the Italian Recovery and Resilience Plan (NRRP) of NextGenerationEU, partnership on "Telecommunications of the Future" (PE00000001 — program "RESTART" CUP: D93C22000910001).

REFERENCES

[1] Zaker, R. and A. Sadeghzadeh, "Passive techniques for target radar cross section reduction: A comprehensive review," *International Journal of RF and Microwave Computer-Aided Engineering*, Vol. 30, No. 11, e22411, 2020.

[2] Skolnik, M. I., *Radar Handbook*, 3rd ed., McGraw-Hill Education, 2008.

[3] Knott, E. F., J. F. Schaeffer, and M. T. Tulley, *Radar Cross Section*, 2nd ed., SciTech Publishing, 2004.

[4] Chen, L., Y. Wang, X. Ye, H. Wang, and S. Tao, "Radar cross section reduction for slot-loaded uav based on characteristic mode theory," in *2021 IEEE International Workshop on Electromagnetics: Applications and Student Innovation Competition (iWEM)*, 1–3, Guangzhou, China, 2021.

[5] Khan, J., W. Duan, and S. Sherbaz, "Radar cross section prediction and reduction for naval ships," *Journal of Marine Science and Application*, Vol. 11, No. 2, 191–199, 2012.

[6] Zheng, B., X. Xiong, J. Tang, and R. Zhang, "Intelligent reflecting surface-aided electromagnetic stealth against radar detection," *IEEE Transactions on Signal Processing*, Vol. 72, 3438–3452, 2024.

[7] Haji-Ahmadi, M.-J., V. Nayyeri, M. Soleimani, and O. M. Ramahi, "Pixelated checkerboard metasurface for ultra-wideband radar cross section reduction," *Scientific Reports*, Vol. 7, No. 1, 11437, 2017.

[8] Azizi, Y., M. Soleimani, S.-H. Sedighy, and L. Matekovits, "Wideband RCS reduction by single-layer phase gradient modulated surface," *Sensors*, Vol. 22, No. 19, 7108, 2022.

[9] Murugesan, A., K. Selvan, A. K. Iyer, K. V. Srivastava, and A. Alphones, "A review of metasurface-assisted RCS reduction techniques," *Progress In Electromagnetics Research B*, Vol. 94, 75–103, 2021.

[10] Zheng, Y., J. Gao, X. Cao, W. Li, T. Liu, and D. Zhang, "Wideband radar cross section reduction covering X and Ku band using artificial magnetic conductor structures," in *2015 IEEE MTT-S International Microwave Workshop Series on Advanced Materials and Processes for RF and THz Applications (IMWS-AMP)*, 1–3, Suzhou, China, 2015.

[11] Yu, N. and F. Capasso, "Flat optics with designer metasurfaces," *Nature Materials*, Vol. 13, No. 2, 139–150, 2014.

[12] Glybovski, S. B., S. A. Tretyakov, P. A. Belov, Y. S. Kivshar, and C. R. Simovski, "Metasurfaces: From microwaves to visible," *Physics Reports*, Vol. 634, 1–72, 2016.

[13] Epstein, A. and G. V. Eleftheriades, "Huygens' metasurfaces via the equivalence principle: Design and applications," *Journal of the Optical Society of America B*, Vol. 33, No. 2, A31–A50, 2016.

[14] Pfeiffer, C. and A. Grbic, "Metamaterial Huygens' surfaces: Tailoring wave fronts with reflectionless sheets," *Physical Review Letters*, Vol. 110, No. 19, 197401, 2013.

[15] Sun, H., C. Gu, X. Chen, Z. Li, L. Liu, B. Xu, and Z. Zhou, "Broadband and broad-angle polarization-independent metasurface for radar cross section reduction," *Scientific Reports*, Vol. 7, No. 1, 40782, 2017.

[16] Achouri, K., M. A. Salem, and C. Caloz, "General metasurface synthesis based on susceptibility tensors," *IEEE Transactions on Antennas and Propagation*, Vol. 63, No. 7, 2977–2991, 2015.

[17] Dai, H., Y. Zhao, J. Chen, C. Yu, and L. Xing, "Ultra-wideband radar cross-section reduction using polarization conversion metasurface," *International Journal of RF and Microwave Computer-Aided Engineering*, Vol. 30, No. 2, e22085, 2020.

[18] Ali, L., Q. Li, T. A. Khan, J. Yi, and X. Chen, "Wideband RCS reduction using coding diffusion metasurface," *Materials*, Vol. 12, No. 17, 2708, 2019.

[19] Tiwari, P., S. K. Pathak, and V. Siju, "Design, development and characterization of resistive arm based planar and conformal metasurfaces for RCS reduction," *Scientific Reports*, Vol. 12, No. 1, 14992, 2022.

[20] Landy, N. I., S. Sajuyigbe, J. J. Mock, D. R. Smith, and W. J. Padilla, "Perfect metamaterial absorber," *Physical Review Letters*, Vol. 100, No. 20, 207402, 2008.

[21] Cui, T. J., M. Q. Qi, X. Wan, J. Zhao, and Q. Cheng, "Coding metamaterials, digital metamaterials and programmable metamaterials," *Light: Science & Applications*, Vol. 3, No. 10, e218, 2014.

[22] Marasco, I., C. Cantore, G. V. Bianco, G. Bruno, A. D'Orazio, and G. Magno, "Transparent graphene-based RIS for 6G communications in the THz spectrum," *IEEE Open Journal of Antennas and Propagation*, Vol. 6, No. 1, 193–200, Feb. 2025.

[23] Magno, G., L. Caramia, G. V. Bianco, G. Bruno, A. D'orazio, and M. Grande, "Design of optically transparent metasurfaces based on CVD graphene for mmWave applications," *Scientific Reports*, Vol. 13, No. 1, 4920, 2023.

[24] Zhu, R., Y. Jia, J. Wang, C. Xu, Z. Meng, S. Sui, Z. Zhang, Y. Zhu, L. Zhang, J. Wang, and S. Qu, "Synthesized optimal design via parallel genetic algorithm of multispectral metasurfaces with ultra-wideband microwave absorption, low infrared emissivity and visible transparency," *Infrared Physics & Technology*, Vol. 117, 103826, 2021.

[25] Ameri, E., S. H. Esmaeli, and S. H. Sedighy, "Ultra wideband radar cross section reduction by using polarization conversion metasurfaces," *Scientific Reports*, Vol. 9, No. 1, 478, 2019.

[26] Zhou, Y., G. Zhang, H. Chen, P. Zhou, X. Wang, L. Zhang, L. Zhang, J. Xie, and L. Deng, "Design of phase gradient coding metasurfaces for broadband wave modulating," *Scientific Reports*, Vol. 8, No. 1, 8672, 2018.

[27] Haupt, R. L. and D. H. Werner, *Genetic Algorithms in Electromagnetics*, John Wiley & Sons, 2007.

[28] Chittur Subramanianprasad, P., Y. Ma, A. A. Ihalage, and Y. Hao, "Active learning optimisation of binary coded metasurface consisting of wideband meta-atoms," *Sensors*, Vol. 23, No. 12, 5546, 2023.

[29] Dobrykh, D., K. Grotov, A. Mikhailovskaya, D. Vovchuk, V. Tkach, M. Khobzei, A. Kharchevskii, A. Glam, and P. Ginzburg, "3D evolutionarily designed metamaterials for scattering maximization," *Communications Engineering*, Vol. 4, No. 1, 40, 2025.

[30] Naseri, P. and S. V. Hum, "A generative machine learning-based approach for inverse design of multilayer metasurfaces," *IEEE Transactions on Antennas and Propagation*, Vol. 69, No. 9, 5725–5739, 2021.

[31] Fowler, C., S. An, B. Zheng, and H. Zhang, "Deep learning for metasurfaces and metasurfaces for deep learning," in *Advances in Electromagnetics Empowered by Artificial Intelligence and Deep Learning*, 319–343, Wiley-IEEE, 2023.

[32] Molesky, S., Z. Lin, A. Y. Piggott, W. Jin, J. Vucković, and A. W. Rodriguez, "Inverse design in nanophotonics," *Nature Photonics*, Vol. 12, No. 11, 659–670, 2018.

[33] Paquay, M., J.-C. Iriarte, I. Ederra, R. Gonzalo, and P. de Maagt, "Thin AMC structure for radar cross-section reduction," *IEEE Transactions on Antennas and Propagation*, Vol. 55, No. 12, 3630–3638, 2007.

[34] Forrester, A., A. Sóbester, and A. Keane, *Engineering Design via Surrogate Modelling: A Practical Guide*, John Wiley & Sons, Chichester, UK, 2008.

[35] Pitilakis, A., M. Seckel, A. C. Tasolamprou, F. Liu, A. Deltsidis, D. Manessis, A. Ostmann, N. V. Kantartzis, C. Liaskos, C. M. Soukoulis, S. A. Tretyakov, M. Kafesaki, and O. Tsilipakos, "Multifunctional metasurface architecture for amplitude, polarization and wave-front control," *Physical Review Applied*, Vol. 17, No. 6, 064060, 2022.

[36] Mahafza, B. R., *Radar Systems Analysis and Design Using MATLAB*, Chapman and Hall/CRC, 2005.

[37] Du, J., Y. Zhao, and W. Qi, "Broadband RCS reduction using single layer random coding polarization conversion metasurface," in *2022 International Applied Computational Electromagnetics Society Symposium (ACES-China)*, 1–2, Xuzhou, China, 2022.

[38] Koziel, S., M. Abdullah, and S. Szczepanski, "Design of high-performance scattering metasurfaces through optimization-based explicit RCS reduction," *IEEE Access*, Vol. 9, 113 077–113 088, 2021.

[39] Ran, Y., L. Shi, S. Wu, J. Li, X. Jin, Z. Hou, B. Fan, and J. Wang, "Optically transparent ultrawideband electromagnetic stealth metasurface for microwave absorption and scattering," *IEEE Antennas and Wireless Propagation Letters*, Vol. 21, No. 12, 2412–2416, 2022.